Available online at www.sciencedirect.com
ScienceDirect
Geochimica et Cosmochimica Acta 70 (2006) 4797–4812
Geochimica
www.elsevier.com/locate/gca

Diffusive fractionation of U-series radionuclides during mantle melting and shallow-level melt–cumulate interaction

James A. Van Orman [a,*], Alberto E. Saal [b], Bernard Bourdon [c], Erik H. Hauri [d]

[a] Department of Geological Sciences, Case Western Reserve University, 10900 Euclid Avenue, Cleveland, OH 44106, USA
[b] Department of Geological Sciences, Brown University, 324 Brook St., Box 1846, Providence, RI 02912, USA
[c] Institut Isotopengeologie/Mineral. Rohstoffe, ETH Zürich, NW D 81.4, Clausiusstrasse 25, 8092 Zürich, Switzerland
[d] Department of Terrestrial Magnetism, Carnegie Institution of Washington, 5241 Broad Branch Road, Washington, DC 20015, USA

Received 12 August 2005; accepted in revised form 11 July 2006

Abstract

U-series radioactive disequilibria in basaltic lavas have been used to infer many important aspects of melt generation and extraction processes in Earth's mantle and crust, including the porosity of the melting zone, the solid mantle upwelling rate, and the melt transport rate. Most of these inferences have been based on simplified theoretical treatments of the fractionation process, which assume equilibrium partitioning of U-series nuclides among minerals and melt. We have developed a numerical model in which solid-state diffusion controls the exchange of U-series nuclides among multiple minerals and melt. First the initial steady-state distribution of nuclides among the phases, which represents a balance between diffusive fluxes and radioactive production and decay, is calculated. Next, partial melting begins, or a foreign melt is introduced into the system, and nuclides are again redistributed among the phases via diffusion. U-series nuclides can be separated during this stage due to differences in their diffusivity; radium in particular, and possibly protactinium as well, can be strongly fractionated from slower-diffusing thorium and uranium. We show that two distinct processes are not required for the generation of ^{226}Ra and ^{230}Th excesses in mid-ocean ridge basalts, as has been argued previously; instead the observed negative correlations of the (^{226}Ra/^{230}Th) activity ratio with (^{230}Th/^{238}U) and with the extent of trace element enrichment may result from diffusive fractionation of Ra from Th during partial melting of the mantle. Alternatively, the (^{226}Ra/^{230}Th) disequilibrium in mid-ocean ridge basalts may result from diffusive fractionation during shallow-level interaction of mantle melts with gabbroic cumulates, and we show that the results of the interaction have a weak dependence on the age of the cumulate if both plagioclase and clinopyroxene are present.

1. Introduction

Intermediate daughters in the U decay chains span a wide range of half-lives and provide a unique geochemical tool for the study of magmatic processes. Activity ratios of U-series nuclides have been used to infer important physical parameters of partial melting processes in Earth's mantle, including solid mantle and melt ascent rates, melting rate, and mantle porosity (Lundstrom et al., 1995; Bourdon et al., 1996; Elliott, 1997; McKenzie, 2000; Lundstrom, 2003; Bourdon and Sims, 2003; Rubin et al., 2005; and references therein). These inferences are based on various theoretical treatments of the fractionation of U-series nuclides during melting and/or transport. The various models differ significantly in their details, and may lead to different conclusions regarding the physical parameters of the melting process. In particular, most U-series fractionation models assume that parent and daughter nuclides are partitioned among minerals and melt in equilibrium proportions during melting and/or transport, neglecting possible kinetic controls on element partitioning. In this paper we show that solid-state diffusion of U-series nuclides may play a strong role in their fractionation during magmatic processes, and present a new model that considers diffusion-controlled exchange of U-series nuclides among the melt and a solid consisting of multiple minerals. We begin by briefly

* Corresponding author. Fax: +1 216 368 3691.
E-mail address: james.vanorman@case.edu (J.A. Van Orman).

0016-7037/$ - see front matter © 2006 Elsevier Inc. All rights reserved.
doi:10.1016/j.gca.2006.07.005

reviewing models for U-series fractionation during partial melting.

The simplest model for the production of U-series disequilibria in melts assumes that nuclides are chemically separated during a single-stage "batch" melting process (Allègre and Condomines, 1982; Sims et al., 1995). U-series nuclides are treated in the same way as trace elements, and the radioactive disequilibria produced depend only on the degree of melting. The "dynamic melting" model (McKenzie, 1985, 2000; Williams and Gill, 1989) takes into account ingrowth of daughters during slow, near-fractional melting, where melt is removed from the system instantly when the melt fraction exceeds a threshold value. In this model, nuclides are fractionated due to differences in their residence time in the solid; the greater residence time of the parent nuclide results in ingrowth of daughters and allows the production of significant radioactive disequilibrium at much higher degrees of melting than in the simple "batch" model. "Equilibrium porous flow" models (Spiegelman and Elliott, 1993; Iwamori, 1994; Lundstrom, 2000; Jull et al., 2002) consider ingrowth of daughter nuclides not only during melting, but also during upward percolation of melts through grain-scale porous networks, which results in general in greater parent–daughter fractionation.

More complicated melting models have been developed to explain two important features of the U-series data set for mid-ocean ridge basalts (MORB) that cannot be explained by simple batch, dynamic melting, or equilibrium porous flow models: (1) a negative correlation between ^{226}Ra excess and ^{230}Th excess; and (2) a negative correlation between ^{226}Ra excess and the incompatible trace element enrichment of the lava. Iwamori (1994) and Lundstrom (2000) developed "two-porosity" melting models in which some melt ascends through grain-scale permeable networks, continuously equilibrating with the solid matrix on the way, and some melt is drawn into high-permeability channels where it ascends rapidly without interacting chemically with the solid matrix. Lundstrom (2000) showed that an apparent discrepancy between U-series data for mid-ocean ridge basalts, which appear to require equilibrium porous flow (e.g., Lundstrom et al., 1995), and trace element data from abyssal peridotites which appear to require disequilibrium transport of melt (Johnson et al., 1990) can be resolved if roughly half the melt is transported by porous flow and half by channel flow. Jull et al. (2002) showed that the negative correlation between ^{226}Ra excess and ^{230}Th excess could be produced by mixing of melts that flowed through channels, carrying with them excess ^{230}Th produced at depth, and percolating melts carrying excess ^{226}Ra produced by equilibrium porous flow. The negative correlation between ^{226}Ra excess and trace element enrichment in mid-ocean ridge basalts has been explained by mixing of melts from different sources (Lundstrom et al., 1999) or different depths within the melting column (Sims et al., 2002), with the low ^{226}Ra in the enriched component resulting from high melt porosities during generation and transport of the melts, or decay during melt transport and storage.

Batch, dynamic melting, equilibrium porous flow and hybrid two-porosity models all assume that partitioning of U-series nuclides among minerals and melt takes place at chemical equilibrium. This condition is met only if the exchange of nuclides between minerals and melt is rapid compared to the rates of melting (or melt transport) and radioactive decay. In the absence of dissolution/precipitation or other short-circuiting processes (e.g., Lundstrom et al., 2005), the rate of mineral–melt chemical exchange is controlled by diffusion in the minerals. If the melting or melt transport rate is very slow compared to radioactive decay, the approach to partitioning equilibrium depends only on the decay and diffusion rates. Partitioning equilibrium can be attained if the diffusion time, r^2/D, where D is the diffusion coefficient and r is the grain radius, is sufficiently short compared to the decay time, $1/\lambda$, where λ is the decay constant. Results of the numerical model described in Saal and Van Orman (2004) indicate that partitioning equilibrium is established between a mineral and melt if the ratio $D/\lambda r^2$ exceeds ~100, and that there is no significant exchange of daughter nuclides between mineral and melt if $D/\lambda r^2$ is less than ~0.001 (Fig. 1). If melting or melt transport is not very slow compared to decay, larger diffusion coefficients are required to attain partitioning equilibrium. For a mantle peridotite with grain radii of 2 mm, complete equilibrium requires diffusion coefficients of at least $\sim 10^{-16}$ m^2/s for ^{230}Th and at least $\sim 5 \times 10^{-15}$ m^2/s for ^{226}Ra. Nuclides with shorter half-lives require even larger diffusion coefficients; for example a diffusion coefficient of $\sim 4 \times 10^{-13}$ m^2/s is required for ^{210}Pb. These values are many orders of magnitude larger than measured and estimated values for clinopyroxene and garnet at pressure–temperature conditions relevant to mantle melting. In high-Ca pyroxene at 1 atm and 1300 °C, for example, the diffusion coefficient for Th is $\sim 2.4 \times 10^{-20}$ m^2/s (Van Orman et al., 1998). At the same conditions, large divalent cations, including Pb, have diffusion coefficients in the range 1.3×10^{-18} to 3.5×10^{-16} m^2/s (Sneeringer et al., 1984; Cherniak, 1998, 2001). The effect of pressure is to decrease diffusion coefficients in minerals; diffusion coefficients for Ce and Yb in high-Ca pyroxene decrease by approximately an order of magnitude between atmospheric pressure and 3.0 GPa (Van Orman et al., 2001). Extrapolated to P–T conditions relevant to the onset of melting beneath mid-ocean ridges, 3 GPa and 1490 °C, the diffusion coefficient for Th in high-Ca pyroxene is $\sim 6 \times 10^{-20}$ m^2/s (see discussion below), which gives $D/\lambda r^2 \sim 0.05$ for grains 2 mm in radius. Equilibrium partitioning thus appears to be a poor assumption if solid-state diffusion is the rate-limiting step in chemical exchange between minerals and melt.

Several previous models have considered the influence of solid-state diffusion on the fractionation of U-series nuclides during melting, but have simplified the problem by treating the solid as a single phase (Qin, 1992; Iwamori,

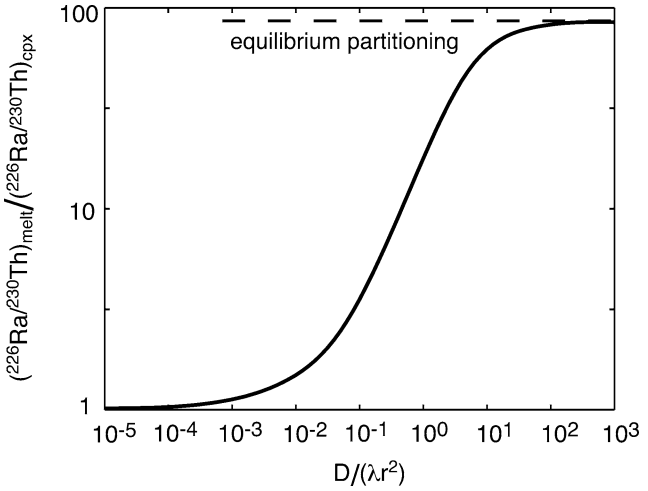

Fig. 1. Model results for decay and exchange of ^{226}Ra and ^{230}Th between a spherical clinopyroxene (cpx) grain and melt, based on the numerical model described in Saal and Van Orman (2004). Initially ^{226}Ra, ^{230}Th and ^{238}U are distributed between the two phases in accordance with their equilibrium partition coefficients. Subsequent decay and diffusive exchange is allowed to proceed for one million years, long enough to establish a steady-state distribution of ^{226}Ra and ^{230}Th between the cpx and melt. The plot shows (^{226}Ra/^{230}Th) in the melt divided by the (^{226}Ra/^{230}Th) in the cpx (integrated over the entire grain), as a function of $(D/\lambda r^2)$, where D is the diffusion coefficient for Ra in the cpx, λ is the decay constant for ^{226}Ra, and r is the radius of the cpx grain. When $(D/\lambda r^2)$ is greater than ~100, ^{226}Ra is able to diffuse out of the cpx grain as quickly as it is produced (by decay of ^{230}Th), allowing the cpx and melt to remain in partitioning equilibrium with respect to ^{226}Ra. When $(D/\lambda r^2)$ is less than ~0.001 no significant exchange of ^{226}Ra between the two phases is possible and the cpx and melt each evolve to a state of secular equilibrium, where (^{226}Ra/^{230}Th) = 1. The curve shown is based on simulations in which the melt fraction is held at 1%, and the cpx/melt partition coefficients are 0.0036 for Th and 4.2×10^{-5} for Ra. The curve shifts to the left for smaller melt fractions or a larger partition coefficient for Ra; in either case it is easier for equilibrium to be established a smaller flux of ^{226}Ra out of the crystal is required. Decreasing the melt fraction to 0.1%, or increasing the Ra partition coefficient by two orders of magnitude, leads to a leftward shift in the curve of approximately one order of magnitude in $(D/\lambda r^2)$.

1994; Van Orman et al., 1998; Saal and Van Orman, 2004). In many situations, more than one mineral is a significant host for U-series nuclides, and in these situations, the distribution of nuclides between minerals must be addressed. Feineman and DePaolo (2003) considered the diffusive exchange of U-series nuclides between minerals in hydrated mantle and found that steady-state radioactive disequilibrium in individual minerals was likely and could potentially influence (^{226}Ra/^{230}Th) activity ratios during partial melting. Here we present a numerical model that addresses not only the initial steady-state distribution of nuclides within and between minerals prior to melting, but also the diffusion-controlled redistribution of nuclides during melting or melt–rock reaction. The numerical model is applied to two different scenarios that are relevant to the production of oceanic basalts: (1) near-fractional adiabatic decompression melting of the mantle (i.e., "dynamic melting") and (2) interaction of mantle melts with gabbroic cumulates as they ascend toward the surface.

2. Model formulation

The model presented here considers diffusion-controlled chemical fractionation of U-series nuclides during adiabatic decompression melting and during melt–rock interaction in the shallow mantle or crust. It is an extension of the diffusion-limited trace element fractionation model of Van Orman et al. (2002), and some aspects of the development and assumptions of the model are discussed in more detail in that paper. The model consists of two steps. First, the initial steady-state distribution of U-series nuclides within and between minerals, prior to melting or melt–cumulate interaction, is calculated. Next, adiabatic decompression melting begins, or a foreign melt is introduced into the system, and nuclides are again redistributed among the phases by solid-state diffusion. During adiabatic decompression melting, we assume that a certain fraction of liquid travels with the upwelling solid, with excess melt drawn into channels and transported instantly to the surface with no further chemical interaction with the solid. Our adiabatic decompression melting model is thus in essence a "dynamic melting" model, with the important difference that our model explicitly considers the diffusion-controlled kinetics of nuclide exchange between minerals and melt rather than assuming equilibrium partitioning *a priori*.

2.1. Initial conditions

When partitioning of nuclides is controlled by diffusion within the minerals, it is necessary to consider the distribution of nuclides within and between mineral grains. In models that assume equilibrium partitioning between minerals and melt, it is not necessary to know how nuclides are distributed among the different minerals in the rock—chemical fractionation of nuclides can be treated simply in terms of the bulk elemental partition coefficients between solid residue and melt. When partitioning of elements is diffusion-controlled, the flux of each nuclide to or from the melt must be considered separately for each mineral. These fluxes depend on the following factors: (i) radioactive production and decay of the nuclide within the mineral; (ii) the nuclide's diffusion coefficient in the mineral; (iii) the mineral–melt partition coefficient, which determines the concentration of the nuclide at the mineral grain's surface; and (iv) the rate of dissolution of the mineral into the melt, which in general is different for each mineral (because melting of the mantle is generally considered to be non-modal). We first consider how nuclides are distributed within and between minerals prior to the onset of melting, and then model their redistribution during partial melting or shallow-level melt–rock interaction.

In many igneous processes, it is reasonable to assume that the bulk rock is in secular equilibrium initially, in which case the atomic ratio of any two nuclides in the decay chain is equal to the ratio of their half-lives. In this paper, secular equilibrium of the bulk rock is assumed to be the initial state prior to partial melting of the mantle. In

a rock in secular equilibrium, the distribution of U-series nuclides within and between minerals is controlled by the production and decay of nuclides within each mineral and by the diffusion-controlled transfer of nuclides between minerals. If a rock remains at constant temperature and pressure for a time on the order of the half-life of the daughter nuclide, a steady state is approached in which production and decay of daughters are balanced by diffusive fluxes. Two extreme scenarios can be envisioned, in which diffusion of daughter nuclides in the minerals is either very sluggish or very rapid compared to their rates of decay. These two scenarios are depicted on an equiline diagram in Fig. 2. In both scenarios we assume that the long-lived parent nuclides ^{238}U and ^{232}Th are distributed among the minerals according to their equilibrium partition coefficients. This is a reasonable assumption for parts of the asthenospheric mantle that have not undergone

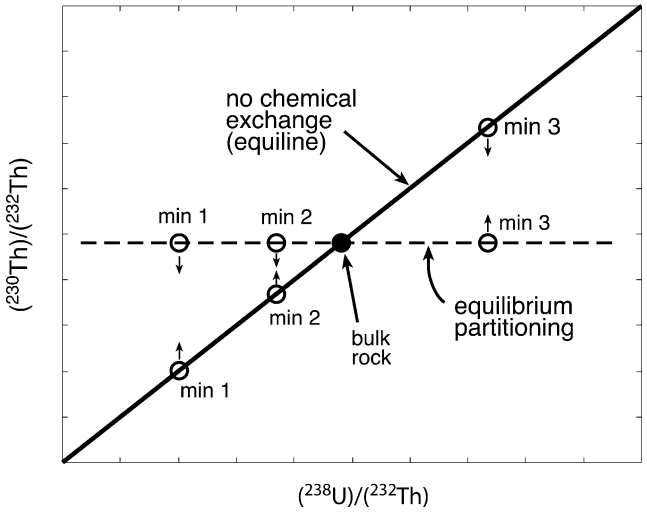

Fig. 2. Schematic equiline diagram illustrating possible steady-state distributions of ^{230}Th and ^{238}U among minerals within a rock that is in bulk secular equilibrium. If the rock has been at high temperature for sufficient time, the long-lived nuclides ^{238}U and ^{232}Th will be exchanged between the minerals by diffusion to achieve an equilibrium distribution. In this case, as depicted in the figure, there will be a dispersion of (^{238}U/^{232}Th) ratios among the minerals in the rock, depending on the relative preference of each mineral for U or Th. The (^{230}Th/^{232}Th) activity ratios in the minerals depend on the relative rates of diffusion and ^{230}Th decay. If diffusion within the minerals is very slow ($D/\lambda_{Th}r^2 \approx 10^{-2}$ or less, where D is the diffusion coefficient for Th in the slowest mineral, and r is the mineral grain radius) there is no exchange of nuclides among the minerals. Because each mineral is effectively a closed system on the timescale of ^{230}Th decay, each mineral evolves to a state of secular equilibrium, with (^{230}Th) = (^{238}U), and mineral compositions thus fall along the one-to-one line known as the equiline (solid). If diffusion is rapid compared to ^{230}Th decay ($D/\lambda_{Th}r^2 \approx 10^2$ or greater), ^{230}Th can be exchanged among the minerals to achieve an equilibrium distribution. In this case all minerals will have the same (^{230}Th/^{232}Th) activity ratio, and thus all mineral compositions will fall along a horizontal line intersecting the bulk composition (dashed line). In intermediate cases, mineral compositions fall between the solid and dashed lines (but do not necessarily fall along a common line). An important point to note is that, even for a rock in bulk secular equilibrium, individual minerals within the rock will generally exhibit daughter excesses or deficits. The only exception is when diffusion in the minerals is very slow compared to the rate of decay of the daughter.

recent partial melting. Diffusion coefficients for U and Th, extrapolated to 3 GPa and 1490 °C (Van Orman et al., 1998, 2001; see discussion below) are on the order of $\sim 6 \times 10^{-20}$ m^2/s. At this rate, spherical clinopyroxene grains 1 mm in radius can exchange U and Th with their surroundings to attain >90% of their ultimate equilibrium values in less than one million years (e.g., Van Orman et al., 1998).

Partitioning of U and Th among minerals that have different preferences for these elements accounts for the dispersion in (^{238}U/^{232}Th) activity ratios along the abscissa in Fig. 1. If diffusion of daughter elements in the minerals is very slow compared to their decay, each mineral is effectively closed to the exchange of daughters and thus plots along the equiline in Fig. 1, indicating that each individual mineral grain is in secular equilibrium. On the other hand, if diffusion is very fast compared to the rate of decay, minerals are able to freely exchange daughter nuclides among themselves. In that case the activity ratios for the minerals fall along a horizontal line that crosses the equiline at the bulk composition; all minerals have the same (^{230}Th/^{232}Th) ratio because ^{230}Th has time to distribute itself among the minerals in equilibrium proportions. When diffusion is neither very fast nor very slow compared to decay, the mineral compositions must fall between the equiline and the horizontal line that crosses it at the bulk composition. In this case mineral grains develop a steady-state zoning in the concentration of daughter nuclides. Feineman and DePaolo (2003) derived an analytical solution for the steady-state distribution of daughters between two phases when diffusion in one of the phases can be treated as infinitely fast. Here we take a numerical approach to the more general problem in which the diffusion rate in each mineral is finite.

We consider a rock comprising several different minerals, and simulate ingrowth, decay, and diffusion-controlled redistribution of daughter nuclides among the minerals. Mineral grains are approximated as spheres, and, for simplicity, each mineral is assumed to have a uniform grain size. The model simulates the evolution of this system toward a steady state, beginning with an equilibrium distribution of the parent nuclide and an arbitrary distribution of daughter nuclides, and stepping forward in time until a steady-state distribution is reached.

Grains of garnet and clinopyroxene, the primary hosts of U-series nuclides in the asthenospheric upper mantle, may not be in physical contact with one another in the mantle, but instead may be separated by olivine (and/or orthopyroxene). The extent to which garnet and clinopyroxene interact with each other chemically depends on the rate of migration of U-series nuclides through grain boundaries; especially olivine grain boundaries. An implicit assumption of our model is that transport through a grain boundary or melt network is so rapid that garnet and clinopyroxene may be treated as being in direct contact over their entire outer boundaries. The same assumption was made by Eiler et al. (1992) with regard to stable isotope interdiffusion in rocks, and by Van Orman et al. (2002)

for diffusion-controlled trace element exchange during mantle melting. Whether the assumption is valid in the case we consider here depends on whether grain boundaries are able to accommodate the flux of U-series daughters—particularly Ra—between garnet and clinopyroxene. This in turn depends on the "carrying capacity" of the grain boundaries (i.e., what concentration of daughter elements the grain boundary region can hold), and on how rapidly the daughters diffuse through the grain boundaries. Hiraga et al. (2004) found that the segregation of large divalent cations to mineral grain boundaries is controlled by strain energy minimization and is well described by an elastic strain model identical to that used for element partitioning between silicate minerals and melts (e.g., Blundy and Wood, 1994). Thus, we assume that the mineral/grain-boundary partition coefficient for Ra is the same as the mineral–melt partition coefficient, and use the partition coefficient for clinopyroxene since this is the primary mineral host for Ra. We consider garnet and clinopyroxene grains to be linked by a grain boundary that can be approximated as a slab with a width of 1 nm, height equal to the diameter of the grains (here assumed to be 4 mm) and length equal to the separation of the grains (assumed to be 10 mm). This grain boundary region is capable of accommodating ~25% of the maximum mass of Ra transferred between clinopyroxene and garnet grains in one time step (833 years) of the simulations discussed below. Thus, the grain boundary region has to be flushed about four times in 833 years in order to accommodate the transfer of Ra between clinopyroxene and garnet; meaning that the diffusion length scale has to be about four times the distance between grains, or about 4 cm. No grain boundary diffusion data are available for Ra or similarly large divalent cations, so we use the "dry" Mg grain boundary diffusion data determined for forsterite (Farver et al., 1994) as a proxy. Of the species that have been studied experimentally, Mg diffuses most slowly through olivine grain boundaries (e.g., Farver and Yund, 2000). The grain boundary diffusion coefficient for Mg, extrapolated to 3 GPa and 1490 °C, is $\sim 4.5 \times 10^{-12}$ m^2/s, and the diffusion length scale over 833 years, $(Dt)^{1/2}$ is ~35 cm. This distance is an order of magnitude longer than necessary to accommodate the diffusive flux of Ra between clinopyroxene and garnet, and thus the fast grain boundary assumption appears to be a reasonable approximation.

In the following, equations are developed specifically for the ^{238}U–^{230}Th–^{226}Ra system that is the primary focus of this paper. We also briefly consider the ^{235}U–^{231}Pa system, and the equations are completely analogous to those given below for ^{238}U and ^{230}Th. Uranium-238 is initially distributed in chemical equilibrium among co-existing phases, with no zoning within mineral grains:

$$C_j^{\mathrm{U}}(r_j, 0) = C_{j,0}^{\mathrm{U}} \quad 0 \leqslant r_j \leqslant R_j, \tag{1}$$

$$\frac{C_{1,0}^{\mathrm{U}}}{K_1^{\mathrm{U}}} = \frac{C_{2,0}^{\mathrm{U}}}{K_2^{\mathrm{U}}} = \cdots = \frac{C_{n,0}^{\mathrm{U}}}{K_n^{\mathrm{U}}}, \tag{2}$$

where $C_j^{\mathrm{U}} = C_j^{\mathrm{U}}(r_j, t)$ is the molar concentration of ^{238}U in a grain of mineral j at a distance r_j from the center, R_j is the grain radius, and K_j^{U} is the partition coefficient for uranium between mineral j and the grain boundary or melt network. As mentioned above, mineral/grain boundary and mineral–melt partition coefficients are assumed to be equal (Hiraga et al., 2004). The only changes in ^{238}U concentrations s are due to decay, and are very small given the short timescale of the simulations (~1 My).

The system as a whole begins in secular equilibrium and remains in secular equilibrium throughout the simulation, such that:

$$M_{\mathrm{Th}}(t) = M_{\mathrm{U}}(t)(\lambda_{\mathrm{U}}/\lambda_{\mathrm{Th}}), \quad M_{\mathrm{Ra}}(t) = M_{\mathrm{U}}(t)(\lambda_{\mathrm{U}}/\lambda_{\mathrm{Ra}}), \tag{3}$$

here M_{U}, M_{Th} and M_{Ra} represent the total number of moles of ^{238}U, ^{230}Th and ^{226}Ra in the system, respectively. To calculate the steady-state distribution of daughter nuclides prior to melting we consider two different starting points, both of which evolve to the same steady-state distribution for the same set of conditions (Fig. 3). In one case, minerals have the same Th and Ra isotopic composition and parent/daughter ratios are controlled by trace element partitioning; and in the second case each mineral grain is assumed to be in secular equilibrium, with the isotopic composition of each mineral plotting along the equiline. In the first case, distributions of ^{230}Th and ^{226}Ra are described by equations analogous to Eqs. (1) and (2), with $C_{j,0}^{\mathrm{Th}}$ and $C_{j,0}^{\mathrm{Ra}}$ determined for each mineral by mass balance using Eq. (3). In the second, distributions are described by:

$$C_j^{\mathrm{Th}}(r_j, 0) = C_{j,0}^{\mathrm{U}}(\lambda_{\mathrm{U}}/\lambda_{\mathrm{Th}}), \quad C_j^{\mathrm{Ra}}(r_j, 0) = C_{j,0}^{\mathrm{U}}(\lambda_{\mathrm{U}}/\lambda_{\mathrm{Ra}}). \tag{4}$$

Diffusion-controlled redistribution of nuclides is described by Fick's second law, modified to account for radioactive production and decay. For each mineral, the concentration as a function of radial position and time is determined by:

$$\begin{aligned}
\frac{\partial C_j^{\mathrm{U}}}{\partial t} &= D_j^{\mathrm{U}}\left(\frac{\partial^2 C_j^{\mathrm{U}}}{\partial r_j^2} + \frac{2}{r_j}\frac{\partial C_j^{\mathrm{U}}}{\partial r_j}\right) - \lambda_{\mathrm{U}} C_j^{\mathrm{U}},\\
\frac{\partial C_j^{\mathrm{Th}}}{\partial t} &= D_j^{\mathrm{Th}}\left(\frac{\partial^2 C_j^{\mathrm{Th}}}{\partial r_j^2} + \frac{2}{r_j}\frac{\partial C_j^{\mathrm{Th}}}{\partial r_j}\right) + \lambda_{\mathrm{U}} C_j^{\mathrm{U}} - \lambda_{\mathrm{Th}} C_j^{\mathrm{Th}},\\
\frac{\partial C_j^{\mathrm{Ra}}}{\partial t} &= D_j^{\mathrm{Ra}}\left(\frac{\partial^2 C_j^{\mathrm{Ra}}}{\partial r_j^2} + \frac{2}{r_j}\frac{\partial C_j^{\mathrm{Ra}}}{\partial r_j}\right) + \lambda_{\mathrm{Th}} C_j^{\mathrm{Th}} - \lambda_{\mathrm{Ra}} C_j^{\mathrm{Ra}},
\end{aligned} \tag{5}$$

where D_j^{U}, D_j^{Th} and D_j^{Ra} are the diffusion coefficients for U, Th and Ra, respectively, in mineral j at the appropriate temperature and pressure. Mineral surfaces are assumed to remain in chemical equilibrium with the grain boundary or melt network at all times:

$$\begin{aligned}
C_j^{\mathrm{U}}(R_j, t) &= K_j^{\mathrm{U}} C_b^{\mathrm{U}}(t),\\
C_j^{\mathrm{Th}}(R_j, t) &= K_j^{\mathrm{Th}} C_b^{\mathrm{Th}}(t),\\
C_j^{\mathrm{Ra}}(R_j, t) &= K_j^{\mathrm{Ra}} C_b^{\mathrm{Ra}}(t),
\end{aligned} \tag{6}$$

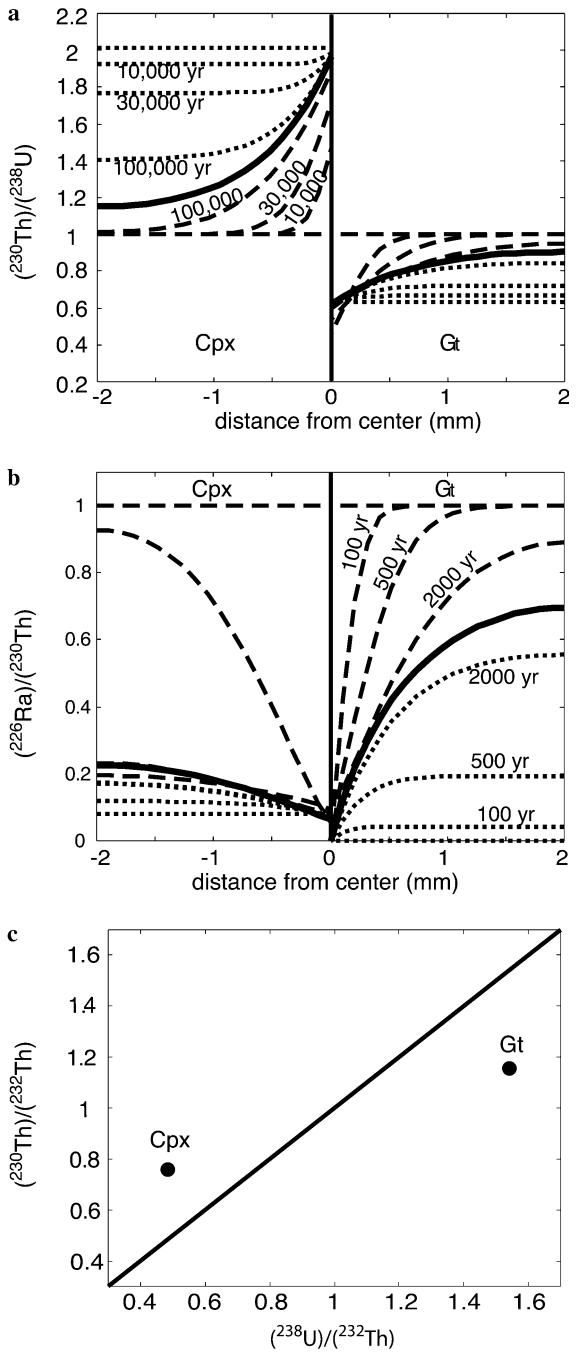

Fig. 3. Steady-state profiles (solid curves) of (a) (^{230}Th/^{238}U) and (b) (^{226}Ra/^{238}U) in spherical high-Ca pyroxene and garnet grains coexisting with a small amount of melt (0.1%) within a garnet peridotite at 3 GPa and 1763 K. Dashed curves show the time evolution of the profiles beginning from an initial state of complete chemical disequilibrium, in which each mineral grain is isolated from the other and internally in secular equilibrium. Dotted curves show the time evolution of the profiles beginning from an initial state in which daughter nuclides are partitioned between the minerals in chemical equilibrium. Each of these two end-member initial distributions converges on the same steady-state profile after several half-lives of the shorter-lived daughter. Panel (c) is an equiline diagram that shows the bulk Th–U isotopic compositions of clinopyroxene and garnet (integrated from core to rim) at steady state. In these simulations the radii of cpx and garnet grains are each 2 mm, and the volume ratio of clinopyroxene to garnet is 2.8.

where C_b^{Th} and C_b^{Ra} are the time-dependent concentrations of Th and Ra, respectively, in the melt or grain boundary network. Concentrations in the grain boundary or melt network are determined by time-dependent mass balance equations:

$$
\begin{aligned}
&\frac{\mathrm{d}}{\mathrm{d}t}\left[\left(\sum_j N_j \int_0^{R_j} 4\pi r_j^2 C_j^{\mathrm{U}}\,\mathrm{d}r_j\right) + V_{\mathrm{m}} C_{\mathrm{m}}^{\mathrm{U}}\right] \\
&\quad = -\lambda_{\mathrm{U}}\left[\left(\sum_j N_j \int_0^{R_j} 4\pi r_j^2 C_j^{\mathrm{U}}\,\mathrm{d}r_j\right) + V_{\mathrm{m}} C_{\mathrm{m}}^{\mathrm{U}}\right], \\
&\frac{\mathrm{d}}{\mathrm{d}t}\left[\left(\sum_j N_j \int_0^{R_j} 4\pi r_j^2 C_j^{\mathrm{Th}}\,\mathrm{d}r_j\right) + V_{\mathrm{m}} C_{\mathrm{m}}^{\mathrm{Th}}\right] \\
&\quad = -\lambda_{\mathrm{Th}}\left[\left(\sum_j N_j \int_0^{R_j} 4\pi r_j^2 C_j^{\mathrm{Th}}\,\mathrm{d}r_j\right) + V_{\mathrm{m}} C_{\mathrm{m}}^{\mathrm{Th}}\right] \\
&\qquad + \lambda_{\mathrm{U}}\left[\left(\sum_j N_j \int_0^{R_j} 4\pi r_j^2 C_j^{\mathrm{U}}\,\mathrm{d}r_j\right) + V_{\mathrm{m}} C_{\mathrm{m}}^{\mathrm{U}}\right], \\
&\frac{\mathrm{d}}{\mathrm{d}t}\left[\left(\sum_j N_j \int_0^{R_j} 4\pi r_j^2 C_j^{\mathrm{Ra}}\,\mathrm{d}r_j\right) + V_{\mathrm{m}} C_{\mathrm{m}}^{\mathrm{Ra}}\right] \\
&\quad = -\lambda_{\mathrm{Ra}}\left[\left(\sum_j N_j \int_0^{R_j} 4\pi r_j^2 C_j^{\mathrm{Ra}}\,\mathrm{d}r_j\right) + V_{\mathrm{m}} C_{\mathrm{m}}^{\mathrm{Ra}}\right] \\
&\qquad + \lambda_{\mathrm{Th}}\left[\left(\sum_j N_j \int_0^{R_j} 4\pi r_j^2 C_j^{\mathrm{Th}}\,\mathrm{d}r_j\right) + V_{\mathrm{m}} C_{\mathrm{m}}^{\mathrm{Th}}\right],
\end{aligned}
\tag{7}
$$

where N_j is the number of grains of mineral j, determined by the mineral proportions and relative grain sizes, and V_{m} is the volume of the grain boundary or melt network, which can be made arbitrarily small. These are simply radioactive decay/production equations integrated over the entire system, and state that the change in mass of an intermediate nuclide in the decay chain is equal to the mass lost by decay plus the mass gained due to decay of the parent.

For a given set of initial conditions, the coupled set of Eqs. (5)–(7) is solved numerically using a Crank–Nicolson finite difference scheme. At each time step, concentration profiles are calculated for all mineral grains simultaneously by inverting a single matrix for each nuclide. The accuracy of the numerical calculation depends on the number of radial grid points and time steps used, and thus there is a tradeoff between accuracy and computation time. For the simulations reported here, we generally used 40 radial grid points and 2000 time steps, and checked the accuracy using a simple mass balance calculation. The total amount of a nuclide in each phase (minerals and melt) at the end of the calculation should agree with the initial amount in the system as a whole. In each simulation these values agreed within less than 2% relative. Use of finer grids improved the agreement, but led to changes of less than a few percent relative in the calculated composition of each phase.

2.2. Adiabatic decompression melting

The basis of the model used to simulate fractionation of U-series nuclides during adiabatic decompression melting is similar to that used to calculate the steady-state distribution of nuclides. Diffusion, production and decay of nuclides within mineral grains are described by Eq. (5), and mineral surfaces are assumed to remain in equilibrium with the residual melt at all times as described by Eq. (6). The initial distribution of nuclides, prior to melting, is the steady-state distribution calculated at the pressure and temperature at which upwelling mantle crosses the solidus and begins to melt. Melt remains with the solid matrix until a critical melt fraction is reached, and is extracted thereafter at a rate that keeps the residual melt fraction constant in volume. Once extracted, melts are assumed to move to the surface instantly, and undergo no further chemical interaction with the solid phases, and no radioactive decay.

The mass balance equations for adiabatic decompression melting are similar to Eq. (7), but include a melt extraction term:

$$\begin{aligned}
&\frac{\mathrm{d}}{\mathrm{d}t}\left[\left(\sum_j N_j \int_0^{R_j} 4\pi r_j^2 C_j^{\mathrm{U}}\,\mathrm{d}r_j\right) + V_{\mathrm{m}} C_{\mathrm{m}}^{\mathrm{U}}\right] \\
&\quad = -\lambda_{\mathrm{U}}\left[\left(\sum_j N_j \int_0^{R_j} 4\pi r_j^2 C_j^{\mathrm{U}}\,\mathrm{d}r_j\right) + V_{\mathrm{m}} C_{\mathrm{m}}^{\mathrm{U}}\right] - \upsilon_{\mathrm{e}} C_{\mathrm{m}}^{\mathrm{U}}, \\
&\frac{\mathrm{d}}{\mathrm{d}t}\left[\left(\sum_j N_j \int_0^{R_j} 4\pi r_j^2 C_j^{\mathrm{Th}}\,\mathrm{d}r_j\right) + V_{\mathrm{m}} C_{\mathrm{m}}^{\mathrm{Th}}\right] \\
&\quad = -\lambda_{\mathrm{Th}}\left[\left(\sum_j N_j \int_0^{R_j} 4\pi r_j^2 C_j^{\mathrm{Th}}\,\mathrm{d}r_j\right) + V_{\mathrm{m}} C_{\mathrm{m}}^{\mathrm{Th}}\right] \\
&\qquad + \lambda_{\mathrm{U}}\left[\left(\sum_j N_j \int_0^{R_j} 4\pi r_j^2 C_j^{\mathrm{U}}\,\mathrm{d}r_j\right) + V_{\mathrm{m}} C_{\mathrm{m}}^{\mathrm{U}}\right] - \upsilon_{\mathrm{e}} C_{\mathrm{m}}^{\mathrm{Th}}, \\
&\frac{\mathrm{d}}{\mathrm{d}t}\left[\left(\sum_j N_j \int_0^{R_j} 4\pi r_j^2 C_j^{\mathrm{Ra}}\,\mathrm{d}r_j\right) + V_{\mathrm{m}} C_{\mathrm{m}}^{\mathrm{Ra}}\right] \\
&\quad = -\lambda_{\mathrm{Ra}}\left[\left(\sum_j N_j \int_0^{R_j} 4\pi r_j^2 C_j^{\mathrm{Ra}}\,\mathrm{d}r_j\right) + V_{\mathrm{m}} C_{\mathrm{m}}^{\mathrm{Ra}}\right] \\
&\qquad + \lambda_{\mathrm{Th}}\left[\left(\sum_j N_j \int_0^{R_j} 4\pi r_j^2 C_j^{\mathrm{Th}}\,\mathrm{d}r_j\right) + V_{\mathrm{m}} C_{\mathrm{m}}^{\mathrm{Th}}\right] - \upsilon_{\mathrm{e}} C_{\mathrm{m}}^{\mathrm{Ra}}.
\end{aligned} \tag{8}$$

Here, υ_{e} is the rate of melt extraction from the solid matrix and V_{m} is the volume of residual melt. Mass balance for each nuclide in the pooled extracted melt is given by

$$\frac{\mathrm{d}V_{\mathrm{M}} C_{\mathrm{M}}^{i}}{\mathrm{d}t} = \upsilon_{\mathrm{e}} C_{\mathrm{m}}^{i}, \tag{9}$$

where V_{M} is the total volume of extracted melt and C_{M}^{i} is the concentration of the nuclide in the aggregated melt. The rate at which melt is extracted from the solid matrix, υ_{e}, stands at zero until the melt fraction reaches a critical value, ϕ_{crit}; thereafter the melt extraction rate is given by:

$$\upsilon_{\mathrm{e}} = \frac{1}{1-\phi_{\mathrm{crit}}}\upsilon_{\mathrm{m}}, \tag{10}$$

where υ_{m} is the melting rate. Note that the melt extraction rate actually exceeds the melting rate after the critical porosity is reached—although the difference is slight as long as the critical porosity is small. A small amount of additional melt needs to be extracted to keep the volume *fraction* of residual melt constant, because the volume of solid decreases as melting proceeds. The melting rate is determined by the upwelling rate W and the melt productivity, $(\partial F/\partial z)$, the fraction of melt produced per meter of adiabatic ascent:

$$\upsilon_{\mathrm{m}} = V_0 W \frac{\partial F}{\partial z}, \tag{11}$$

where V_0 is the initial solid volume, defined as $\sum_j N_j 4/3\pi (R_{j,0})^3$. We use a simple melt productivity function based on MELTS calculations for near-fractional melting of fertile peridotite (Asimow et al., 1995, 1997). At pressures above 1.0 GPa the productivity is constant at 0.02 GPa^{-1}, with the exception of a short interval near the garnet-spinel transition (2.5–2.475 GPa) where the melt productivity drops to zero. At pressures below 1.0 GPa the productivity increases linearly at 0.717 GPa^{-2}.

As melting progresses the volume of each solid phase changes according to $\frac{\mathrm{d}V_j}{\mathrm{d}t} = -\alpha_j \upsilon_{\mathrm{m}}$, where α_j is the stoichiometric coefficient of phase j in the melting reaction. Solid grains preserve their spherical symmetry as they dissolve, and the number of grains in the system is fixed. For the numerical calculations, a fixed number of radial grid points is maintained for each mineral grain, and the moving grain boundary is accommodated by rescaling the grid to the new grain radius R_j at each time step. The moving grain boundary was dealt with in the same way by Van Orman et al. (2002) in modeling diffusive fractionation of trace elements, and the numerical results were found to agree with analytical solutions for melting under conditions of complete chemical equilibrium and complete chemical disequilibrium. For simulations in which melting begins in the garnet stability field, garnet disappears at a pressure of 2.5 GPa and releases its nuclides to the residual melt, where they then re-partition into the minerals to the extent that diffusion allows. In the simulations presented below, the initial volume fraction of garnet and cpx, and their stoichiometric coefficients in the melting reaction, are the same as those used in the models presented by Van Orman et al. (2002).

2.3. Melt–cumulate interaction

Saal and Van Orman (2004) considered the effects of diffusive exchange with shallow-level cumulates on the U-series compositions of enriched and depleted oceanic basalts. In that paper the problem was simplified by considering interaction with plagioclase-dominated (troctolitic) and clinopyroxene-dominated (wehrlitic) cumulates. Here we consider interaction with gabbroic cumulates that

contain both clinopyroxene and plagioclase. We assume the cumulates crystallized in chemical equilibrium with an average MORB with a uranium concentration of 150 ppb, (^{230}Th/^{238}U) activity ratio of 1.13 and (^{226}Ra/^{230}Th) ratio of 1.0. After crystallization, the cumulate may or may not develop steady-state nuclide distributions, depending on how much time is available between crystallization of the cumulate and its diffusive interaction with a foreign melt. We consider cumulates with a full range of ages, from zero-age to steady state.

We also consider the perhaps more realistic case in which a continuous flux of melt passes through the cumulate zone. Following crystallization, successive batches of fresh melt, all with the same composition as the original melt, are introduced into the cumulate zone and each allowed to interact diffusively with the cumulate minerals for a certain period of time. The reaction time is equivalent to the residence time for melts within the cumulate zone, which is calculated to be 500 years for a melt flux of 400 m^2/yr through a cumulate zone 20 km wide and 1 km deep, with 1% porosity. A melt flux of 400 m^2/yr is appropriate for mid-ocean ridges, consistent with the formation of 6 km of basaltic crust at a mid-ocean ridge with 7 cm/yr half-spreading rate. After a series of ~10 melt batches have been flushed through the cumulate zone, (over 5000 years) the system converges to a steady state in which successive batches of melt approach a steady post-reaction composition. The distribution of U-series nuclides among the minerals at this point is assumed to be the initial distribution prior to the introduction of a foreign (more or less depleted) melt into the cumulate zone.

We assume that no dissolution or crystallization of minerals occurs during interaction between cumulates and foreign melts. Although it is generally expected that crystallization or dissolution will accompany the interaction of cumulates with foreign melts, in most cases these are expected to have little effect on the results. It can be shown through a simple mass balance calculation that for the cases considered here in which the porosity is on the order of 1%, the ^{226}Ra isotopic composition of even the most depleted basalts will change only slightly (less than 10% relative) even when the melt dissolves an amount of high-Ca pyroxene or plagioclase equal to its own mass. This effect is negligible compared to the influence of diffusive exchange, which may involve the entire volume of a mineral grain rather than only the outermost rim.

2.4. Diffusion and partition coefficients

The diffusion coefficient for nuclide i in mineral j is assumed to vary exponentially with temperature and pressure according to:

$$D^i_j = D^i_{0,j} \exp\left(\frac{-(E^i_j + PV^i_j)}{RT}\right),$$

where R is the gas constant, D_0 is the diffusion coefficient extrapolated to infinite temperature, E is the activation energy and V is the activation volume. Shallow-level melt–rock reaction processes are assumed here to be isothermal and isobaric, and the diffusion coefficients used for U, Th and Ra in plagioclase (Table 1) are the same as those discussed in Saal and Van Orman (2004). Diffusion parameters for U and Th in high-Ca pyroxene were derived from the 1 atm experimental data of Van Orman et al. (1998), and we assumed an activation volume for both elements of 10 cm^3/mol, similar to the experimental values determined for Ce and Yb in high-Ca pyroxene (Van Orman et al., 2001). Diffusion parameters for Ra^{2+} in high-Ca pyroxene were estimated using an elastic model (Van Orman et al., 2001). According to this model a suite of cations with the same valence, diffusing by the same mechanism, has a parabolic dependence of ln$D$ on ionic radius, with a parameter b controlling the curvature of the parabola. We assumed b for divalent cations to be 2/3 the value determined for trivalent cations (Van Orman et al., 2001) and estimated the diffusion coefficient for Ra at 1 atm and 1200 °C by fitting to the elastic model all existing data for Sr and Pb in high-Ca pyroxene (Sneeringer et al., 1984; Cherniak, 1998, 2001). We did not include diffusion data for Ca because, unlike the larger divalent cations, it has been found to diffuse by an interstitial mechanism (Dimanov et al., 1996), which is not expected for Ra given its large ionic radius. There is wide (~2 log units) scatter in the diffusion coefficients for Pb and Sr in different high-Ca pyroxene compositions, leading to a relatively large uncertainty in the estimated diffusivity for Ra. However, even at the low end of the estimated range, Ra diffusivity is at least an order of magnitude faster than U or Th. The activation energy for Ra was calculated according to the model described in Van Orman et al. (2001). No diffusion data exist for Pa or any other 5+ cations in clinopyroxene, and thus any estimate of its diffusivity must be regarded as crude. We used the elastic model described by Van Orman et al. (2001) to estimate diffusion parame-

Table 1
Diffusion parameters

	D_0^{Cpx} (m^2/s)	E^{Cpx} (kJ/mol)	V^{Cpx} (cm^3/mol)	D_0^{Gt} (m^2/s)	E^{Gt} (kJ/mol)	V^{Gt} (cm^3/mol)	$D^{Plag}_{1200°C}$ (m^2/s)
U	1.8×10^{-6}	418	10	4.7×10^{-10}	295	10	3.2×10^{-21}
Th	1.7×10^{-8}	356	10	4.7×10^{-10}	295	10	3.1×10^{-21}
Ra	2.9×10^{-3}	430	10	8.1×10^{-10}	245	10	6.9×10^{-19}
Pa	5.2×10^{-6}	402	10	3.6×10^{-10}	320	10	—

Table 2
Partition coefficients

	K^{Cpx} (mantle)	K^{Cpx} (gabbro)	K^{Gt}	K^{Plag}
U	0.0049	0.018	0.055	0.0006
Th	0.0036	0.021	0.013	0.0020
Ra	4.2×10^{-5}	4.2×10^{-5}	10^{-9}	0.049
Pa	4.9×10^{-8}	—	3.5×10^{-4}	—

ters for Pa, assuming it occupies the M2 site (Blundy and Wood, 2003) and that the migration energy increases linearly with ionic charge. According to this model, Pa is predicted to diffuse about an order of magnitude faster than U and Th at the pressures and temperatures of interest due to its smaller radius—despite its higher charge.

In garnet, diffusion coefficients have been found to depend strongly on ionic charge but weakly on ionic radius (e.g., Van Orman et al., 2002). We assumed that the diffusivity of Ca (Chakraborty and Ganguly, 1992; Freer and Edwards, 1999; Carlson, 2002) was a reasonable proxy for Ra, and estimated diffusion parameters for U, Th and Pa by extrapolating linearly from values determined for Ca and Sm (Van Orman et al., 2002) in pyrope-rich garnets. Activation volumes for all elements were assumed to be 10 cm^3/mol, similar to experimentally determined values for Mg in alumino-silicate garnets (Chakraborty and Rubie, 1996). At mantle solidus conditions, U and Th diffusion coefficients estimated for garnet are similar to those in high-Ca pyroxene. Ra diffusivity in garnet is estimated to be an order of magnitude slower than in high-Ca pyroxene, but still nearly two orders of magnitude faster than U and Th.

The partition coefficients used in the simulations are listed in Table 2. Cpx/melt partition coefficients used for adiabatic decompression melting of the upper mantle represent values near the mantle solidus at high pressure (Blundy and Wood, 2003). Plag/melt and Cpx/melt partition coefficients used for gabbro/melt interaction are the same as those used by Saal and Van Orman (2004). Garnet/melt partition coefficients for U and Th are taken from the experimental results of Salters et al. (2002), and the partition coefficients for Ra and Pa are calculated values reported by Blundy and Wood (2003). It should be noted that the model results are insensitive to the precise value of the partition coefficient when the mineral–melt partition coefficient is very small (less than $\sim10^{-4}$), as it is for Pa and Ra in cpx and garnet.

3. Model results and discussion

3.1. Adiabatic decompression melting

Figs. 4 and 5 show U-series activity ratios in the residual and aggregated melt as functions of the total degree of partial melting. Melting in these simulations is nearly fractional, with 0.2% melt remaining with the solid matrix, and begins in the garnet stability field at 3.0 GPa and 1490 °C. In these simulations the transition from garnet peridotite to spinel peridotite occurs when the total melt fraction reaches 1%. At approximately 4% melting the melt productivity begins to increase sharply, as described above, from an initial value of 0.02 to 0.38 GPa^{-1} at the top of the melting column. Diffusion coefficients in high-Ca pyroxene decrease by approximately an order of magnitude from the bottom of the melting column to the top; the effect of decreasing temperature outweighs the effect of decreasing pressure. The increase in melt productivity (which increases the melting rate) and decrease in diffusivity both lead to an increasing degree of chemical disequilibrium between the minerals and residual melt as melting progresses. This has the effect of increasing the effective mineral–melt partition coefficients of incompatible elements, toward an ultimate value of 1 when no exchange of elements between minerals and melt is possible. Uranium and thorium are affected more strongly than Pa and Ra because they diffuse more slowly, and this leads to strong diffusive fractionation of Ra/Th and Pa/U. The effects on residual melt composition are illustrated in Fig. 4. At melting degrees below ~1%, the ($^{226}Ra/^{230}Th$) and ($^{231}Pa/^{235}U$) activity ratios decrease with increasing melt fraction. This reflects the usual behavior of highly incompatible elements, which are significantly fractionated only at low melt fractions when partitioning equilibrium is maintained. As the melting rate increases from 1 cm/yr to 10 cm/yr, the drop in ($^{226}Ra/^{230}Th$) and ($^{231}Pa/^{235}U$) activity ratios at low melt fractions becomes less severe, due to an increase in the effective partition coefficients for Th and U, while the effective partition coefficients for Ra and Pa remain small. At higher degrees of melting, ($^{226}Ra/^{230}Th$) and ($^{231}Pa/^{235}U$) begin to increase, again reflecting strong diffusive fractionation of Ra/Th and Pa/U, with steeper increases at higher mantle upwelling rates. The ($^{226}Ra/^{230}Th$) and (presup231Pa/^{235}U) activity ratios reach a peak value and begin to decrease at higher melt fractions, between ~4% and 12%. The decreasing activity ratios reflect weaker fractionation of Ra/Th and Pa/U when the melting rate becomes so high that Ra and Pa are unable to diffuse out of the minerals efficiently, and their effective partition coefficients, like those of U and Th, also begin to approach a value of 1.

Fig. 5 shows activity ratios in the aggregated melt as a function of the total degree of melting. Although the composition of the aggregated melt at the top of the melting column (to the right of the figure) is dominated by deep melts, shallow melts make a larger contribution than in models that assume equilibrium partitioning of U-series nuclides. Incompatible elements are lost from the solid less efficiently when partitioning is diffusion-limited, and thus are present in higher abundance at shallower levels; their higher concentrations give them more leverage in affecting the composition of the aggregate melt. As the upwelling rate increases, the degree of disequilibrium increases, and shallow melts have a progressively greater influence on the composition of the aggregated melt.

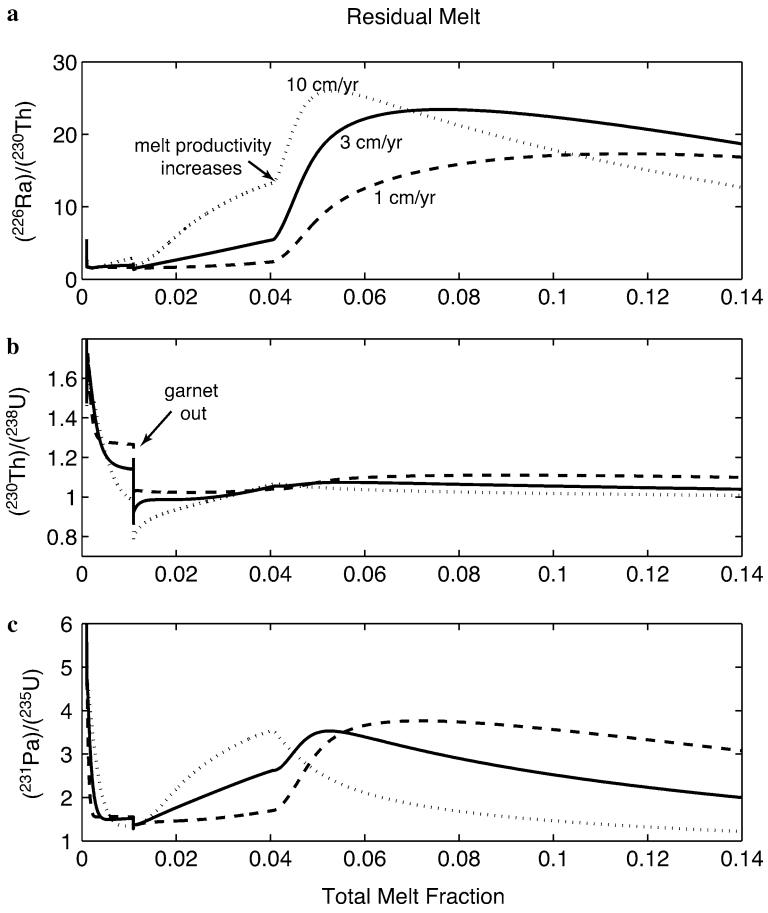

Fig. 4. Results of disequilibrium mantle melting simulations showing activity ratios in the residual melt as a function of the total degree of melting. In all simulations melting begins in the garnet stability field at 3 GPa and ceases at 0.5 GPa, with a residual porosity of 0.2%. The transition from garnet peridotite to spinel peridotite occurs at a melt fraction of ~1%, and the melt productivity begins to increase at a melt fraction of ~4%. The results of three different simulations are shown, for solid mantle upwelling rates of 1 cm/yr (dashed curves), 3 cm/yr (solid curves) and 10 cm/yr (dotted curves). The initial solid is in bulk secular equilibrium, with steady-state distributions of daughter nuclides between garnet and cpx grains 2 mm in radius.

Fig. 5 also shows that (^{226}Ra/^{230}Th) and (^{231}Pa/^{235}U) activity ratios in the final aggregated melt increase with the mantle upwelling rate, while (^{230}Th/^{238}U) ratios decrease with upwelling rate. Thorium and uranium are fractionated from each other less efficiently at higher upwelling rates, because the more compatible element, U, has a slightly higher diffusivity. Rapid upwelling also leaves less time for the ^{230}Th ingrowth in the solid, and this also inhibits the production of large ^{230}Th excesses in the melt. Fig. 6 shows the covariation of (^{226}Ra/^{230}Th) and (^{230}Th/^{238}U) in the final aggregated melt over a broader range of conditions, and compares the model results with U-series data for mid-ocean ridge basalts from the East Pacific Rise. Each curve shows calculated activity ratios for a series of melts, each representing an aggregate over the entire mantle melting column, with each point along the curve corresponding to a different mantle upwelling rate, between 0.3 and 30 cm/yr. Each of the three curves corresponds to a different initial depth (pressure) of melting, 3.0, 2.7 or 2.5 GPa. The (^{230}Th/^{238}U) activity ratio depends strongly on the initial depth of melting, which determines the proportion of melt derived from garnet peridotite. ^{230}Th excesses are generated even when melting begins within the spinel peridotite stability field at 2.5 GPa because of the slightly more compatible behavior of U compared to Th in clinopyroxene at high pressure (Blundy and Wood, 2003). The (^{226}Ra/^{230}Th) activity ratio also depends strongly on the initial depth of melting. When melting begins at shallower depths, a greater proportion of the melting takes place at shallow levels where the melt productivity is high and diffusive fractionation of Ra and Th is strong. Thus the (^{226}Ra/^{230}Th) activity ratio tends to be larger when melting begins at shallower depths.

The model results shown in Fig. 6 reproduce the negative correlation between (^{230}Th/^{238}U) and (^{226}Ra/^{230}Th) observed in mid-ocean ridge basalts and encompass most of the MORB data (lower (^{226}Ra/^{230}Th) ratios may be explained by decay during melt transport, which is not considered in the model). However, these results do not provide an explanation for the negative correlation between (^{226}Ra/^{230}Th) ratio and the trace element enrichment of the basalt, since the model aggregate melts all have very similar trace element (U and Th) concentrations. To address this correlation we consider a simple two-component

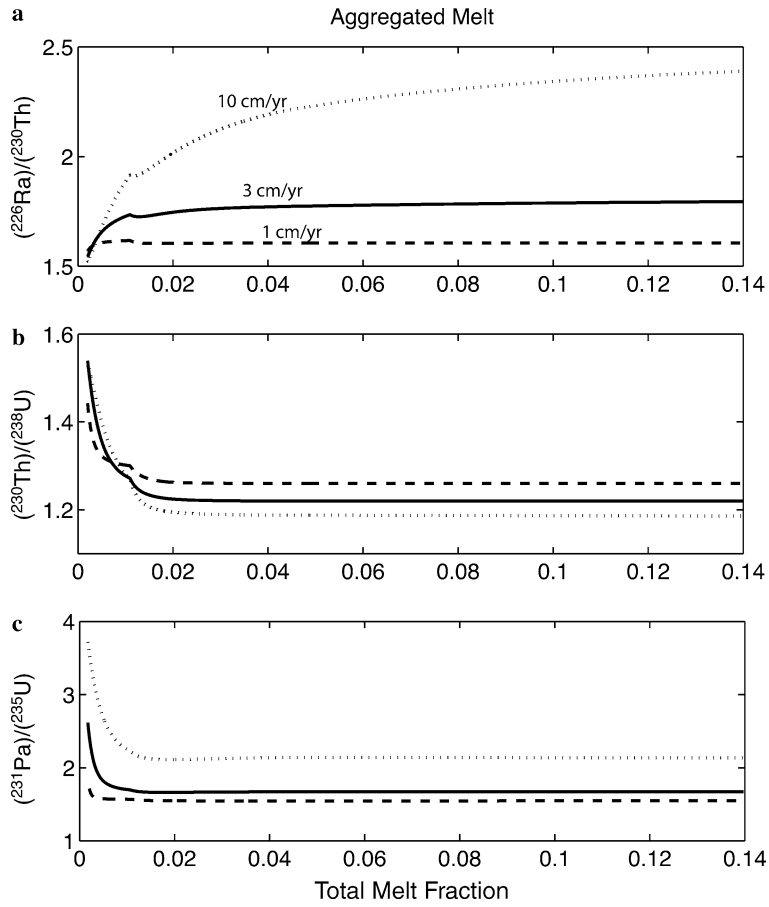

Fig. 5. Activity ratios in the aggregated melt as a function of the total degree of melting, for the same set of simulations shown in Fig. 4. The aggregated melt consists of a mixture of all melts that have been extracted from the system at the given degree of melting. Melts are assumed to be extracted and transported instantly in the absence of any radioactive decay.

mixing model in which the end-member melts are derived from different depth ranges in the melting column. Fig. 7 shows mixing curves between two components, one of which is an aggregated melt derived from pressures of 3.0 to 2.0 GPa (representing a total of 2% melting), and the other an aggregated melt from the pressure range 2.0–0.5 GPa (representing 12% melting). These pressure ranges are arbitrary, but were chosen such that the melt components encompass the range of trace element (uranium) enrichment observed in mid-ocean ridge basalts. Broadly similar results are obtained for many other two-component mixtures of deep and shallow melts. The deep component is enriched in trace elements (~950–1000 ppb U), has relatively high (^{230}Th/^{238}U) activity ratios (~1.2–1.25) and moderate (^{226}Ra/^{230}Th) ratios (~1.5–2). The shallow component is depleted (<10 ppb U), has little or no ^{230}Th excess, and has a wide range of (^{226}Ra/^{230}Th) ratios depending on the mantle upwelling rate. Mixing lines between the deep and shallow components have negative slopes on a plot of (^{226}Ra/^{230}Th) vs. (^{230}Th/^{238}U), and roughly parallel the trend of the MORB data at an upwelling rate of 3 cm/yr (Fig. 7a).

Mixing of deep and shallow melts also results in an inverse correlation between (^{226}Ra/^{230}Th) and trace element enrichment (Fig. 7b), with most of the MORB data bracketed by models with upwelling rates between 3 and 10 cm/yr. It should be emphasized that the negative correlation between ^{226}Ra excess and U enrichment in this model is a direct result of diffusive fractionation during melting—not during melt transport (we assume no decay during transport). Mixing of deep and shallow melts has been called on before to explain MORB data (Lundstrom et al., 1999; Sims et al., 2002; Jull et al., 2002), but the end-member melts in these models have a different origin than in our model. In prior models the lack of ^{226}Ra excess in the enriched end-member was inferred to be the result of high melt porosities during melt generation and/or decay during melt transport and storage. In our model, all melts are produced at the same critical melt porosity, and we assume no decay during melt transport. However, allowing ^{226}Ra to decay during ascent, with ascent rates on the order of ~50 m/yr, would bring the mixing curves shown in Fig. 7 into better agreement with the MORB data.

In order for our melting model to reproduce the ^{226}Ra excess observed in MORB, melts must ascend from ~60 km depth to the surface in less than about 2000 years. Greater melt ascent times would cause ^{226}Ra excesses to decay to levels lower than observed, and would require a

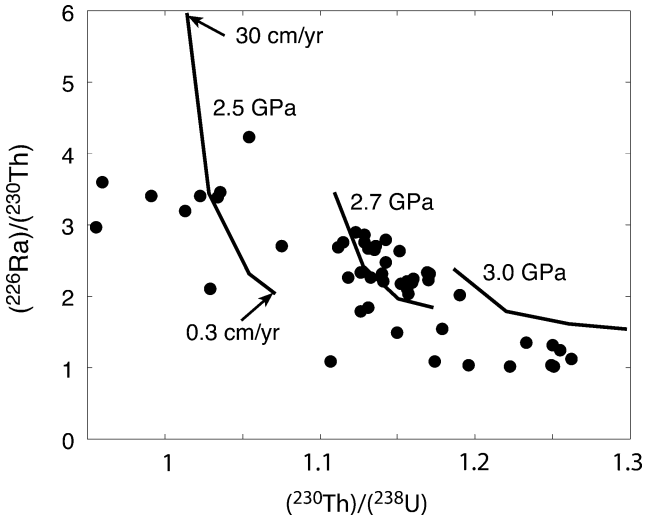

Fig. 6. Comparison of (^{226}Ra/^{230}Th) and (^{230}Th/^{238}U) data for mid-ocean ridge basalts (Lundstrom et al., 1999; Sims et al., 2002; Volpe and Goldstein, 1993; Goldstein et al., 1989, 1991, 1993; Tepley et al., 2004) with calculated aggregate melts generated at different upwelling rates, and different initial depths of melting. Each curve shows calculated melt compositions for solid upwelling rates ranging from 0.3 cm/yr (lower right) to 30 cm/yr (upper left). The labels on each of the three curves indicate the pressure at which melting begins (3.0 and 2.7 GPa are within the garnet stability field, 2.5 GPa is within the spinel stability field); in each case melting ceases at 0.5 GPa. A small melt fraction (0.2%) remains with the solid during melting, and excess melt is removed and aggregated instantly (there is no decay of nuclides during melt transport). As in the simulations shown in Figs. 4 and 5, the intial grain radii are 2 mm, and the initial volume ratio of clinopyroxene to garnet is 2.8.

separate process to explain the ^{226}Ra excess in MORB. One possibility is that the ^{226}Ra excesses in MORB are produced by shallow-level melt–cumulate interaction, as discussed by Saal and Van Orman (2004). In the next section we take the modeling of Saal and Van Orman (2004) a step further by considering interaction with gabbroic cumulates that contain both clinopyroxene and plagioclase, not just one or the other.

Table 3
Melt compositions prior to and following diffusive interaction with a gabbro crystallized from a MORB with 150 ppb U, (^{230}Th/^{238}U) = 1.13, and (^{226}Ra/^{230}Th) = 1.00

Initial melt			Final melt (after 500 yrs diffusive interaction)		
U (ppb)	[^{230}Th/^{238}U]	[^{226}Ra/^{230}Th]	U (ppb)	[^{230}Th/^{238}U]	[^{226}Ra/^{230}Th]
8.0	0.715	1.00	12.1	1.064	6.060
13.3	0.850	1.00	16.8	1.068	4.503
28.3	1.017	1.00	31.4	1.106	2.569
38.0	1.071	1.00	41.0	1.126	2.056
51.5	1.12	1.00	54.1	1.153	1.652
77.3	1.176	1.00	79.2	1.192	1.262
98.8	1.203	1.00	100.1	1.204	1.097
197.5	1.259	1.00	196.4	1.249	0.794
484.0	1.280	1.00	475.5	1.262	0.621
988.0	1.278	1.00	966.3	1.259	0.560

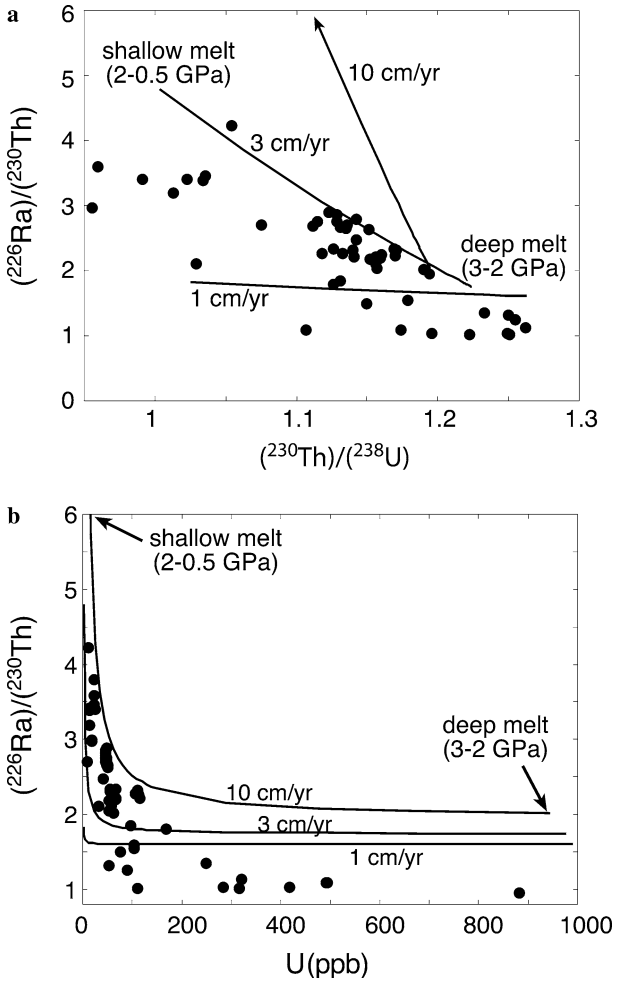

Fig. 7. Comparison of data for mid-ocean ridge basalts (Lundstrom et al., 1999; Sims et al., 2002; Volpe and Goldstein, 1993; Goldstein et al., 1989, 1991, 1993; Tepley et al., 2004) with a two-component mixing model. The two components are a deep aggregate of melts derived from pressures of 3.0–2.0 GPa and a shallow aggregate of melts from 2.0 to 0.5 GPa. Parameters of the melting model are the same as those used to generate the results shown in Fig. 6. (a) (^{226}Ra/^{230}Th) versus (^{230}Th/^{238}U). Mixing lines between calculated shallow and deep melts are shown for solid mantle upwelling rates of 1, 3 and 10 cm/yr. The trend of the MORB data is roughly parallel to the mixing line for melts generated at a solid upwelling rate of 3 cm/yr. The half-spreading rate along the East Pacific Rise at 9–10 °N, where most of the MORB data come from, is ~5 cm/yr, and the mantle upwelling rate should be similar if flow is passive. (b) (^{226}Ra/^{230}Th) versus U content. Most of the MORB data are encompassed by mixing curves for upwelling rates between 3 and 10 cm/yr. The mixing curves may overestimate the (^{226}Ra/^{230}Th) activity ratios because they do not account for decay during melt transport and storage.

3.2. Melt–cumulate interaction

We simulated melt–cumulate interaction between a gabbro comprising 40% clinopyroxene, 30% plagioclase and 30% olivine, crystallized from an average NMORB, and a series of more and less depleted melts. One series of simulations, discussed below, explored the influence of cumulate age on the composition of the interacting melt. All other simulations involved a gabbro that, as described in Section 2.3, had been conditioned by a continuous flux of

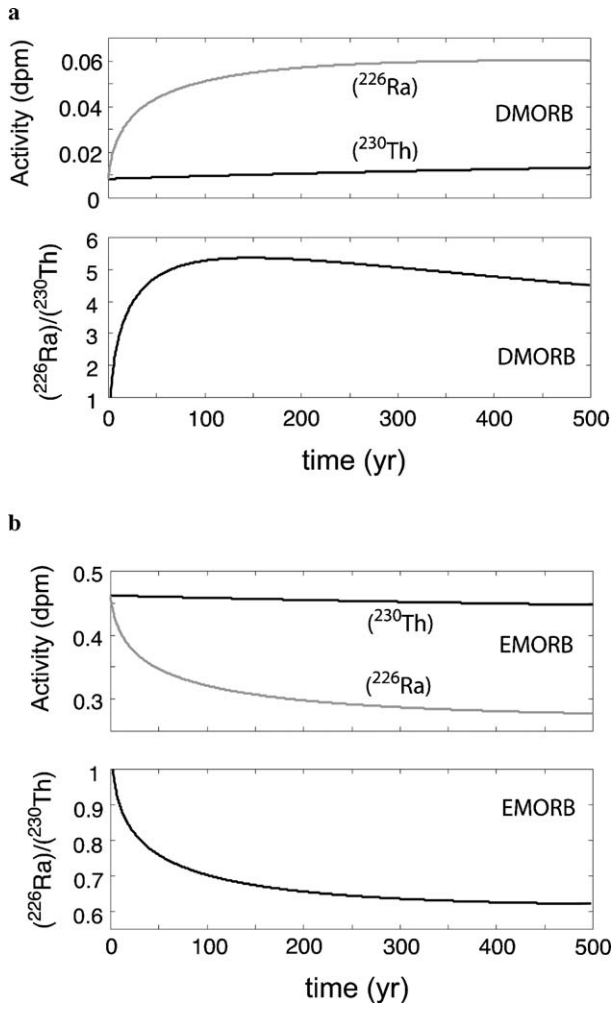

Fig. 8. Calculated results of diffusive interaction between oceanic basalts and gabbroic cumulates crystallized from an average NMORB, and conditioned by a steady flux of fresh batches of average NMORB until a steady state is reached. The results are displayed as ^{226}Ra and ^{230}Th activities and [^{226}Ra/^{230}Th] activity ratios in the melt versus interaction time. In case (a) a depleted (DMORB) melt (13.3 ppb U; see Table 3), and in case (b) an enriched (EMORB) melt (484 ppb U) interact with the gabbro. The gabbro consists of 40% cpx, 30% plag, 30% olivine, with 0.25 mm grain radii, the interacting melt fraction is 1%, and the temperature is 1200 °C. As discussed in the text, the estimated residence time for melts in the cumulate interaction zone is 500 years.

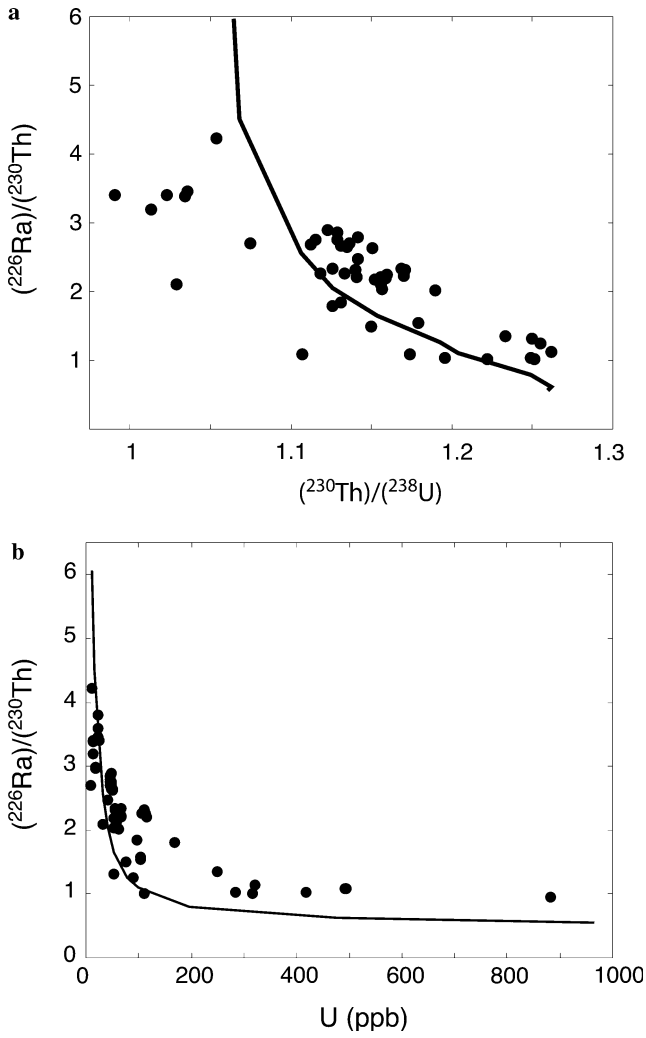

Fig. 9. Comparison of mid-ocean ridge basalt data (Lundstrom et al., 1999; Sims et al., 2002; Volpe and Goldstein, 1993; Goldstein et al., 1989, 1991, 1993; Tepley et al., 2004) with the results of our shallow-level gabbro interaction model. The results are displayed as (a) (^{226}Ra/^{230}Th) versus (^{230}Th/^{238}U), and (b) (^{226}Ra/^{230}Th) versus U content. Model results represent melts that have undergone diffusive interaction with a gabbroic cumulate, conditioned by a steady flux of average NMORB, for 500 years. Initial and final melt compositions are listed in Table 3. Model parameters are the same as those used for the calculations shown in Fig. 8.

average NMORB prior to the introduction of a more or less depleted melt. Initial and final compositions of melts interacting with this pre-conditioned steady-state gabbro are listed in Table 3. The initial (^{226}Ra/^{230}Th) ratios in the interacting melts were all assumed to equal one, and the initial (^{230}Th/^{238}U) activity ratios were chosen to approximate the trend of (^{230}Th/^{238}U) versus uranium enrichment observed in mid-ocean ridge basalts (Lundstrom et al., 1999; Sims et al., 2002; Volpe and Goldstein, 1993; Goldstein et al., 1989, 1991, 1993; Tepley et al., 2004).

Fig. 8 shows the evolution of (^{226}Ra/^{230}Th) and (^{230}Th/^{238}U) activity ratios in DMORB and EMORB melts as they interact with the gabbro for 500 years. ^{226}Ra and ^{230}Th diffuse from the gabbro into the DMORB melt and from the EMORB melt into the gabbro in an attempt to reach partitioning equilibrium. Because Ra diffuses much faster than Th, the (^{226}Ra/^{230}Th) activity ratio in the DMORB increases, and the (^{226}Ra/^{230}Th) activity ratio in the EMORB decreases. Fig. 9 shows that an NMORB gabbro interacting with melts having a wide range in enrichment results in a negative correlation between (^{226}Ra/^{230}Th) and (^{230}Th/^{238}U) in the melts, and also a negative correlation between (^{226}Ra/^{230}Th) and the trace element enrichment.

A fundamental difference between the present model and the model previously published by Saal and Van Orman (2004) is that the age of the cumulate has a much

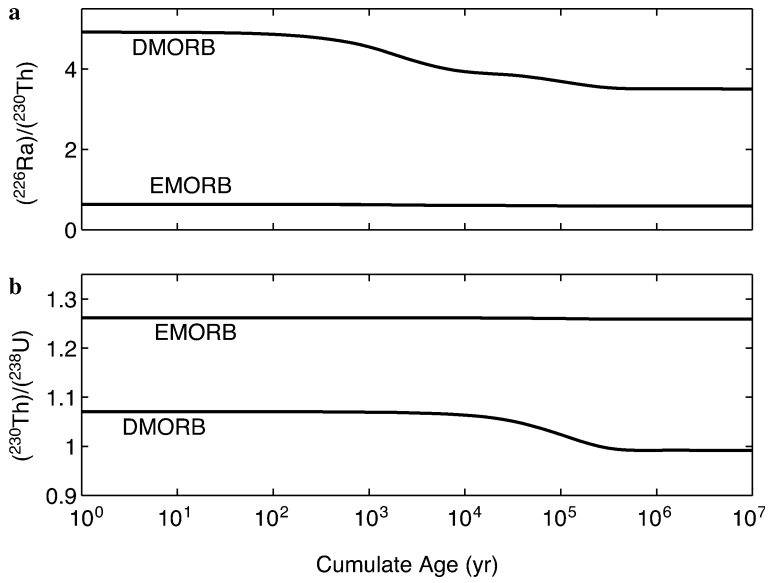

Fig. 10. Calculated (a) (^{226}Ra/^{230}Th) and (b) (^{230}Th/^{238}U) activity ratios in DMORB and EMORB melts following 500 years of diffusive interaction with gabbroic cumulates of various ages, crystallized in equilibrium with average NMORB. The age of the cumulate has a modest influence on (^{226}Ra/^{230}Th) and (^{230}Th/^{238}U) activity ratios in DMORB, and a very small influence on the activity ratios in EMORB. Clinopyroxene, which is relatively enriched in ^{238}U and ^{230}Th, provides a steady source of ^{226}Ra, allowing co-existing plagioclase to maintain high ^{226}Ra abundances even in very old gabbros.

smaller influence on the results in the case we consider here. In the Saal and Van Orman (2004) model it was necessary that the clinopyroxene be old (allowing ^{226}Ra to accumulate in clinopyroxene by decay of ^{230}Th) and that the plagioclase be young (avoiding decay of unsupported ^{226}Ra) in order for melt–cumulate interaction to reproduce the trends observed in oceanic basalts. Young clinopyroxene or old plagioclase contained insufficient ^{226}Ra to produce high (^{226}Ra/^{230}Th) ratios in depleted basalts. When both clinopyroxene and plagioclase are present in the cumulate, the age has only a second order influence on the composition of the interacting melt (Fig. 10). Plagioclase dominates the behavior of the system because it hosts the bulk of the ^{226}Ra. Clinopyroxene is relatively enriched in ^{230}Th, which decays to provide a steady source of ^{226}Ra for absorption by the plagioclase. The presence of clinopyroxene allows plagioclase to maintain high ^{226}Ra activity even in an old gabbro that has attained a steady-state distribution of U-series nuclides.

4. Conclusions

We have presented a numerical model to describe diffusion-controlled fractionation of U-series nuclides during mantle melting and shallow-level melt–cumulate interaction. Radium is inferred to diffuse much more rapidly than U and Th in clinopyroxene, garnet and plagioclase, due to the strong negative dependence of diffusivity on ionic charge in these minerals, and this may lead to strong diffusive fractionation of divalent ^{226}Ra from its tetravalent parents. Protactinium is also tentatively inferred to have a higher diffusivity than U or Th, due to its significantly smaller ionic radius, and thus is expected to behave similarly to Ra. We find that:

(1) Diffusive fractionation can produce large ^{226}Ra and ^{231}Pa excesses in the aggregated melt during adiabatic decompression melting, in the absence of chemical exchange during melt percolation at shallow levels.
(2) Under conditions relevant to melting beneath mid-ocean ridges, the ^{226}Ra excess in the aggregated melt increases with solid mantle upwelling rate and is negatively correlated with the ^{230}Th excess.
(3) Mixing of deep and shallow melts results in inverse correlations of (^{226}Ra/^{230}Th) ratio with (^{230}Th/^{238}U) and with trace element enrichment, similar to the trends observed in mid-ocean ridge basalts. In the present model all melts are produced by the same process, and at the same critical melt porosity; thus we conclude that separate melting processes or melt transport regimes are not required to explain these correlations.
(4) Diffusive exchange with gabbroic cumulates may have a strong influence on the (^{226}Ra/^{230}Th) activity ratio of the melt, and may also lead to negative correlations of (^{226}Ra/^{230}Th) with (^{230}Th/^{238}U), and with the extent of trace element enrichment.

Acknowledgments

We wish to acknowledge Aaron Pietruszka, Craig Lundstrom and Tim Elliott for excellent reviews that improved the manuscript considerably, and Peter Kelemen and Ken Sims for helpful comments and suggestions. This material

is based upon work supported by the National Science Foundation under Grants No. 0337125 and 0322766 (J.V.).

Associate editor: Alan D. Brandon

References

Allègre, C.J., Condomines, M., 1982. Basalt genesis and mantle structure studied through Th-isotopic geochemistry. *Nature* **299**, 21–24.

Asimow, P.D., Hirschmann, M.M., Ghiorso, M.S., O'Hara, M.J., Stolper, E.M., 1995. The effect of pressure-induced solid-solid phase transitions on decompression melting of the mantle. *Geochim. Cosmochim. Acta* **59**, 4489–4506.

Asimow, P.D., Hirschmann, M.M., Stolper, E.M., 1997. An analysis of variations in isentropic melt productivity. *Philos. Trans. R. Soc. Lond.* **A355**, 244–281.

Blundy, J.D., Wood, B.J., 1994. Prediction of crystal–melt partition coefficients from elastic moduli. *Nature* **372**, 452–454.

Blundy, J.D., Wood, B.J., 2003. Mineral–melt partitioning of uranium, thorium and their daughters. *Rev. Mineral. Geochem.* **52**, 59–118.

Bourdon, B., Sims, K.W., 2003. U-series constraints on intraplate basaltic magmatism. *Rev. Mineral. Geochem.* **52**, 215–253.

Bourdon, B., Zindler, A., Elliott, T., Langmuir, C.H., 1996. Constraints on mantle melting at mid-ocean ridges from global U-238-Th-230 disequilibrium data. *Nature* **384**, 231–235.

Carlson, W.D., 2002. Scales of disequilibrium and rates of equilibration during metamorphism. *Am. Mineral.* **87**, 185–204.

Chakraborty, S., Ganguly, J., 1992. Cation diffusion in aluminosilicate garnets: experimental determination in spessartine–almandine diffusion couples, evaluation of effective binary diffusion coefficients, and applications. *Contrib. Mineral. Petrol.* **111**, 74–86.

Chakraborty, S., Rubie, D.C., 1996. Mg tracer diffusion in aluminosilicate garnets at 750–850 °C, 1 atm and 1300 °C, 8.5 GPa. *Contrib. Mineral. Petrol.* **122**, 406–414.

Cherniak, D.J., 1998. Pb diffusion in clinopyroxene. *Chem. Geol.* **150**, 105–117.

Cherniak, D.J., 2001. Pb diffusion in Cr diopside, augite, and enstatite, and consideration of the dependence of cation diffusion in pyroxene on oxygen fugacity. *Chem. Geol.* **177**, 381–397.

Dimanov, A., Jaoul, O., Sautter, V., 1996. Calcium self-diffusion in natural diopside single crystals. *Geochim. Cosmochim. Acta* **60**, 4095–4106.

Eiler, J.M., Baumgartner, L.P., Valley, J.W., 1992. Intercrystalline stable isotope diffusion: a fast grain boundary model. *Contrib. Mineral. Petrol.* **112**, 543–557.

Elliott, T., 1997. Fractionation of U and Th during mantle melting: a reprise. *Chem. Geol.* **139**, 165–183.

Farver, J.R., Yund, R.A., 2000. Silicon diffusion in forsterite aggregates: implications for diffusion accommodated creep. *Geophys. Res. Lett.* **27**, 2337–2340.

Farver, J.R., Yund, R.A., Rubie, D.C., 1994. Magnesium grain boundary diffusion in forsterite aggregates at 1000 and 1300 °C and 0.1 MPa to 10 GPa. *J. Geophys. Res.* **99**, 19809–19819.

Feineman, M.D., DePaolo, D.J., 2003. Steady-state $^{226}Ra/^{230}Th$ disequilibrium in mantle minerals: implications for melt transport rates in island arcs. *Earth Planet. Sci. Lett.* **215**, 339–355.

Freer, R., Edwards, A., 1999. An experimental study of Ca-(Fe,Mg) interdiffusion in silicate garnets. *Contrib. Mineral. Petrol.* **134**, 370–379.

Goldstein, S.J., Murrell, M.T., Janecky, D.E., 1989. Th and U isotopic systematics of basalts from the Juan de Fuca and Gorda Ridges by mass spectrometry. *Earth Planet. Sci. Lett.* **96**, 134–146.

Goldstein, S.J., Murrell, M.T., Janecky, D.E., Delaney, J.R., 1991. Geochronology and petrogenesis of MORB from the Juan de Fuca and Gorda Ridges by ^{238}U–^{230}Th disequilibrium. *Earth Planet. Sci. Lett.* **107**, 25–41.

Goldstein, S.J., Murrell, M.T., Williams, R.W., 1993. ^{231}Pa and ^{230}Th chronology of mid-ocean ridge basalts, Earth Planet. *Sci. Lett.* **115**, 151–159.

Hiraga, T., Anderson, I.M., Kohlstedt, D.L., 2004. Grain boundaries as reservoirs of incompatible elements in the Earth's mantle. *Nature* **427**, 699–703.

Iwamori, H., 1994. ^{238}U–^{230}Th–^{226}Ra and ^{235}U–^{231}Pa disequilibria produced by mantle melting with porous and channel flows. *Earth Planet. Sci. Lett.* **125**, 1–16.

Johnson, K.T.M., Dick, H.J.B., Shimizu, N., 1990. Melting in the oceanic upper mantle: an ion microprobe study of diopsides in abyssal peridotites. *J. Geophys. Res.* **95**, 2661–2678.

Jull, M., Kelemen, P.B., Sims, K.W., 2002. Consequences of diffuse and channeled porous melt migration on uranium series disequilibria. *Geochim. Cosmochim. Acta* **66**, 4133–4148.

Lundstrom, C., Boudreau, A., Pertermann, M., 2005. Diffusion-reaction in a thermal gradient: Implications for the genesis of anorthitic plagioclase, high alumina basalt and igneous mineral layering. *Earth Planet. Sci. Lett.* **237**, 829–854.

Lundstrom, C.C., Gill, J., Williams, Q., Perfit, M.R., 1995. Mantle melting and basalt extraction by equilibrium porous flow. *Science* **270**, 1958–1961.

Lundstrom, C.C., Sampson, D.E., Perfit, M.R., Gill, J., Williams, Q., 1999. Insights into mid-ocean ridge basalt petrogenesis: U-series disequilibria from the Siqueiros Transform, Lamont Seamounts, and East Pacific Rise. *J. Geophys. Res.* **104**, 13035–13048.

Lundstrom, C.C., 2000. Model of U-series disequilibria generation in MORB: the effects of two scales of melt porosity. *Phys. Earth Planet. Interiors* **121**, 189–204.

Lundstrom, C.C., 2003. Uranium-series disequilibria in mid-ocean ridge basalts: Observations an dmodels of basalt genesis. *Rev. Mineral. Geochem.* **52**, 175–212.

McKenzie, D., 1985. ^{230}Th–^{238}U disequilibrium and the melting processes beneath ridge axes. *Earth Planet. Sci. Lett.* **72**, 149–157.

McKenzie, D., 2000. Constraints on melt generation and transport from U-series activity ratios. *Chem. Geol.* **162**, 81–94.

Qin, Z., 1992. Disequilibrium partial melting model and its implications for trace element fractionations during mantle melting. *Earth Planet. Sci. Lett.* **109**, 611–620.

Rubin, K.H., van der Zander, I., Smith, M.C., Bergmanis, E.C., 2005. Minimum speed limit for ocean ridge magmatism from ^{210}Pb–^{226}Ra–^{230}Th disequilibria. *Nature* **437**, 534–538.

Saal, A.E., Van Orman, J.A., 2004. The ^{226}Ra enrichment in oceanic basalts: evidence for melt–cumulate diffusive interaction processes within the oceanic lithosphere. *Geochem. Geophys. Geosyst.* **5**, Paper # 2003GC000620.

Salters, V.J.M., Longhi, J.E., Bizimis, M., 2002. Near mantle solidus trace element partitioning at pressures up to 3.4 GPa. *Geochem. Geophys. Geosyst.* **3**, Paper # 2001GC000148.

Sims, K.W.W., DePaolo, D.J., Murrell, M.T., Baldridge, W.S., Goldstein, S.J., Clague, D., 1995. Mechanism of magma generation beneath Hawaii and mid-ocean ridges: uranium/thorium and samarium/neodymium isotopic evidence. *Science* **267**, 508–512.

Sims, K.W.W., Goldstein, S.J., Blichert-Toft, J., Perfit, M., Kelemen, P.B., Fornari, D., Michael, P.J., Murrell, M.T., Hart, S.R., DePaolo, D.J., Layne, G., Ball, L., Jull, M., Bender, J., 2002. Chemical and isotopic constraints on the genesis and transport of magmas beneath the East Pacific Rise. *Geochim. Cosmochim. Acta* **66**, 3481–3505.

Sneeringer, M., Hart, S.R., Shimizu, N., 1984. Strontium and samarium diffusion in diopside. *Geochim. Cosmochim. Acta* **48**, 1589–1608.

Spiegelman, M., Elliott, T., 1993. Consequences of melt transport for U-series disequilibrium in young lavas. *Earth Planet. Sci. Lett.* **118**, 1–20.

Tepley III, F.J., Lundstrom, C.C., Sims, K.W.W., Hékinian, R., 2004. U-series disequilibria in MORB from the Garrett Transform and implications for mantle melting. *Earth Planet. Sci. Lett.* **223**, 79–97.

Van Orman, J.A., Grove, T.L., Shimizu, N., 1998. Uranium and thorium diffusion in diopside. *Earth Planet. Sci. Lett.* **160**, 505–519.

Van Orman, J.A., Grove, T.L., Shimizu, N., 2001. Rare earth element diffusion in diopside: influence of temperature, pressure and ionic

radius, and an elastic model for diffusion in silicates. *Contrib. Mineral. Petrol.* **141**, 687–703.

Van Orman, J.A., Grove, T.L., Shimizu, N., 2002. Diffusive fractionation of trace elements during production and transport of melt in Earth's upper mantle. *Earth Planet. Sci. Lett.* **198**, 93–112.

Volpe, A.M., Goldstein, S.J., 1993. ^{226}Ra–^{230}Th disequilibrium in axial and off-axis mid-ocean ridge basalts. *Geochim. Cosmochim. Acta* **57**, 1233–1241.

Williams, R.W., Gill, J.B., 1989. Effects of partial melting on the ^{238}U decay series. *Geochim. Cosmochim. Acta* **53**, 1607–1619.